I – A hydrodynamical clone of the Virgo cluster of galaxies to confirm observationally driven formation scenarios

Jenny G. Sorce, Yohan Dubois, Jérémy Blaizot, Sean L. Mcgee, Gustavo Yepes, Alexander Knebe

Monthly Notices of the ROYAL ASTRONOMICAL SOCIETY

MNRAS **504,** 2998–3012 (2021) doi:10.1093/mnras/stab1021
Advance Access publication 2021 April 15

I – A hydrodynamical CLONE of the Virgo cluster of galaxies to confirm observationally driven formation scenarios

Jenny G. Sorce,[1,2]★ Yohan Dubois,[3] Jérémy Blaizot,[4] Sean L. McGee,[5] Gustavo Yepes[6,7] and Alexander Knebe[6,7,8]

[1]*Univ Lyon, ENS de Lyon, Univ Lyon1, CNRS, Centre de Recherche Astrophysique de Lyon UMR5574, F-69007 Lyon, France*
[2]*Leibniz-Institut für Astrophysik, An der Sternwarte 16, D-14482 Potsdam, Germany*
[3]*Institut d'Astrophysique de Paris, UMR 7095 CNRS et Université Pierre et Marie Curie, 98bis Bd Arago, F-75014 Paris, France*
[4]*Univ Lyon, Univ Lyon1, Ens de Lyon, CNRS, Centre de Recherche Astrophysique de Lyon UMR5574, F-69230 Saint-Genis-Laval, France*
[5]*School of Physics and Astronomy, University of Birmingham, Edgbaston, Birmingham B15 2TT, UK*
[6]*Departamento de Física Teórica, Universidad Autónoma de Madrid, Cantoblanco, E-28049 Madrid, Spain*
[7]*Centro de Investigación Avanzada en Física Fundamental, Facultad de Ciencias, Universidad Autónoma de Madrid, E-28049 Madrid, Spain*
[8]*International Centre for Radio Astronomy Research, University of Western Australia, 35 Stirling Highway, Crawley, Western Australia 6009, Australia*

Accepted 2021 April 9. Received 2021 March 12; in original form 2020 December 7

ABSTRACT

At ∼16–17 Mpc from us, the Virgo cluster is a formidable source of information to study cluster formation and galaxy evolution in rich environments. Several observationally driven formation scenarios arose within the past decade to explain the properties of galaxies that entered the cluster recently and the nature of the last significant merger that the cluster underwent. Confirming these scenarios requires extremely faithful numerical counterparts of the cluster. This paper presents the first CLONE, Constrained LOcal and Nesting Environment, simulation of the Virgo cluster within a ∼15 Mpc radius sphere. This cosmological hydrodynamical simulation, with feedback from supernovae and active galactic nuclei, with a $\sim 3 \times 10^7$ $M_\odot$ dark matter particle mass and a minimum cell size of 350 pc in the zoom region, reproduces Virgo within its large-scale environment unlike a random cluster simulation. Overall the distribution of the simulated galaxy population matches the observed one including M87. The simulated cluster formation reveals exquisite agreements with observationally driven scenarios: within the last Gyr, about 300 small galaxies ($M^* > 10^7$ $M_\odot$) entered the cluster, most of them within the last 500 Myr. The last significant merger event occurred about 2 Gyr ago: a group with a tenth of the mass of today's cluster entered from the far side as viewed from the Milky Way. This excellent numerical replica of Virgo will permit studying different galaxy type evolution (jellyfish, backsplash, etc.) as well as feedback phenomena in the cluster core via unbiased comparisons between simulated and observed galaxies and hot gas phase profiles to understand this great physics laboratory.

Key words: hydrodynamics – methods: numerical – galaxies: clusters: general – galaxies: evolution – galaxies: formation.

1 INTRODUCTION

Since 1936, no less than a thousand titles of publications posted on the Astrophysics Data System contain the words 'Virgo cluster', among which more than half are refereed articles. Unconditionally, the Virgo cluster of galaxies, by its proximity with us, has largely been studied both observationally and numerically. The list of papers is long and citing all these papers is unconceivable even if they all deserve some credit. To name a few, we can mention the first paper available in the archive from 1936 that already gave an estimate of the mass of the cluster (Smith 1936). Quickly the focus turned to dwarf galaxies and their great importance to really understand the cluster's contents (Reaves 1956). Then the interest grew towards the (dynamical) distribution of galaxies and the structure of the cluster (e.g. de Vaucouleurs 1961; Holmberg 1961) to understand its formation and the evolution of galaxies once they enter this dense environment. Nowadays, the cluster still arouses a lot of interest, explaining the wide diversity seen in a large number of observational projects: e.g. Binggeli & Huchra (2000) for a book review; e.g. Wong & Kenney (2009) and Karachentsev et al. (2014) for Spitzer and Hubble studies; Roediger et al. (2011a, b) and Lee et al. (2016) for multiwavelength studies; e.g. Boselli et al. (2011, 2014, 2016a) and Vollmer et al. (2012) for the GUViCS survey; e.g. Fritz & Hevics Collaboration (2011) and Pappalardo et al. (2015) for the Herschel Virgo cluster surveys; and e.g. Taylor et al. (2012) and Ferrarese et al. (2016) for the NGVS survey. We can also mention the black hole (BH) of M87, its central galaxy, that became lately famous with the Event Horizon Telescope observations (e.g. Event Horizon Telescope Collaboration 2019a, b). There is also a growing number of numerical modelling to understand the cluster (e.g. Hoffman, Olson & Salpeter 1980; Corbett Moran, Teyssier & Lake 2014; Li & Gnedin 2014; Zhu et al. 2014, for a non-exhaustive list), but none of these studies to our knowledge both set the cluster within its large-scale environment and included baryonic physics. Clearly questions are still arising and a complete picture of the formation and evolution of the Virgo cluster remains to be validated.

★ E-mail: jenny.sorce@univ-lyon1.fr

Indeed, although Virgo is recognized as a dynamically young and unrelaxed cluster with its quite large number of substructures (e.g. Huchra 1985; Binggeli, Tammann & Sandage 1987), completely understanding the full formation history of the cluster and the evolution of galaxies, once inside this dense environment, from today observations, is largely based on assumptions that require to be tested against modelling. However, the diversity of clusters in terms of morphologies, formation history, etc. (Struble & Rood 1988), makes the one-to-one comparison observed versus simulated clusters a daunting task. An alternative consists in reproducing directly the Virgo cluster rather than selecting a cluster among a set of random simulated clusters. Bertschinger (1987) proposed first that option suggesting to constrain the initial conditions of cosmological simulations, namely the Gaussian field, to reproduce rare objects such as massive clusters. The importance of the large-scale environment on the formation of the cluster, later implied the necessity of simulating the cluster in its large-scale environment. Namely, the necessity of being able to simulate our cosmic neighbourhood, the local Universe, arose.

Nowadays, several techniques have the ability to reproduce the local large-scale structure (e.g. Dekel, Bertschinger & Faber 1990; Hoffman & Ribak 1991, 1992; Ganon & Hoffman 1993; Bistolas & Hoffman 1998; Zaroubi, Hoffman & Dekel 1999; Kitaura & Enßlin 2008; Lavaux et al. 2008; Jasche & Wandelt 2013; Kitaura 2013; Wang et al. 2014; Lavaux 2016). However, reaching a precision of a few Megaparsecs to constrain also the clusters, at the linear/non-linear threshold limit is not immediate (see e.g. Sorce 2018). Recently, Sorce et al. (2016b) proposed new initial conditions constrained with local observational data that lead to dark matter-only cosmological simulations resembling the local Universe that are in addition valid down to the Virgo cluster scale. Further studies of these dark matter-only simulations (Sorce et al. 2016b; Sorce, Blaizot & Dubois 2019) proved the robustness of these initial conditions: resulting simulated Virgo clusters present the same type of merging history, including the preferential accretion direction predicted by observations (West & Blakeslee 2000), with properties like the centre of mass offset with respect to the spherical centre, restricted to a given range of values when compared to random simulated clusters in the same mass range. These counterparts of the observed Virgo cluster appear as exceptional tools to check the observationally driven formation scenarios more thoroughly once baryons are included.

Numerous hypotheses regarding the formation of the cluster and the evolution of the galaxies once they entered it indeed remain uncertain. For instance, Boselli et al. (2008) estimated the infall within the Virgo cluster to be about 300 galaxies with stellar mass above 10^7 $M_\odot$ per Gyr within the last few Gyr. This infall rate might explain the large amount of galaxies rapidly becoming red (Boselli & Gavazzi 2014) with galaxies that entered the inner cluster within the last 500 Myr (Boselli et al. 2016b). Recently, Lisker et al. (2018) found indications of a recent group infall into the Virgo cluster, of about 10 per cent of the mass of the cluster, within the last few Gyr. This finding is in excellent agreement with the predictions from the dark matter-only simulations of the Virgo cluster obtained earlier on. Indeed, Olchanski & Sorce (2018) concluded their analysis with the last significant merger, about 10 per cent the cluster mass, occurred within the last few Gyr. This further strong agreement between our dark matter-only constrained simulations and the observationally driven formation scenarios reinforces the argument in favour of simulating a Virgo counterpart with full hydrodynamics and baryons to check that these findings hold with baryonic matter and to push further the comparisons.

Indeed, if a clear link between galaxy population and the high density of a cluster environment has been established over the past few years (e.g. Avila-Reese et al. 2005; Maulbetsch et al. 2007; Hirschmann et al. 2014), further investigations revealed that the history of the cluster plays an equal role on the baryonic phase at both the hot gas level and the galaxy population level (Hahn et al. 2017). To fully understand these reservoirs of galaxies or cosmic laboratories to finally use them as cosmological probes, comparisons must be legitimate. There is no room for biases. First and foremost, this first paper of a series confirms in deeper details that the simulated Virgo cluster shares with its observed counterpart similar galaxy distribution at $z = 0$ and formation history.

This paper presents the first CLONE, Constrained LOcal and Nesting Environment, simulation of the Virgo cluster: a full-zoom hydrodynamical simulation of the Virgo cluster counterpart, as shown in Fig. 1, obtained with initial conditions constrained only with local galaxy peculiar velocities, namely the Virgo cluster counterpart was not added as an extra density constraint in its forming region. This specificity permits controlling not only the presence of the cluster in its large-scale environment at $z = 0$ but also its formation history. In the following, when not specified, Virgo will refer to the observed Virgo cluster. This zoom-in simulation of the Virgo cluster is the first one of its kind and it was produced with the adaptive mesh refinement RAMSES code (Teyssier 2002). The first section describes the properties of this simulation as well as the building of its initial conditions. The second part of the paper cross-checks the simulated galaxy population distribution against that of the observed Virgo cluster at $z = 0$ and highlights M87 and its simulated counterpart. The last section before concluding confronts observationally driven formation scenarios and numerical ones.

2 THE SIMULATION

Different papers described at length the construction of the constrained initial conditions and the hydrodynamical features used to evolve these initial conditions. This section thus only summarizes the main concepts regarding the constrained aspect to get a Virgo counterpart and the hydrodynamical aspect to get a realistic galaxy population. It also gives the run properties.

2.1 Constrained initial conditions

In a previous study, we built 200 realizations of the initial conditions of the local Universe that all form a Virgo cluster counterpart (Sorce et al. 2019). The details of the steps to produce these constrained initial conditions can be found in Sorce et al. (e.g. 2016b). The local observational data used to constrain the initial conditions are 3D peculiar velocities (Sorce et al. 2014) derived with a Wiener filter technique (Fisher et al. 1995) from a distance catalogue of local galaxies (Tully et al. 2013) that are mainly grouped (e.g. Sorce & Tempel 2017; Sorce, Hoffman & Gottlöber 2017), bias minimized (Sorce 2015), and relocated to their progenitors position using the reverse Zel'dovich approximation (Doumler et al. 2013) to form the local clusters at $z = 0$ (Sorce 2018).

The detailed study of the 200 simulated Virgos presented in Sorce et al. (2019) showed that all of our counterparts share a similar historical behaviour and properties with a smaller variance than would have a random set of haloes within the same mass range. Additionally, they have clearly distinct features from any set of random haloes of the same size. For instance, while the random haloes have an average velocity of 463 ± 207 km s^{-1}, Virgo counterparts have an average velocity of 646 ± 79 km s^{-1} barely within the 1σ range of the random

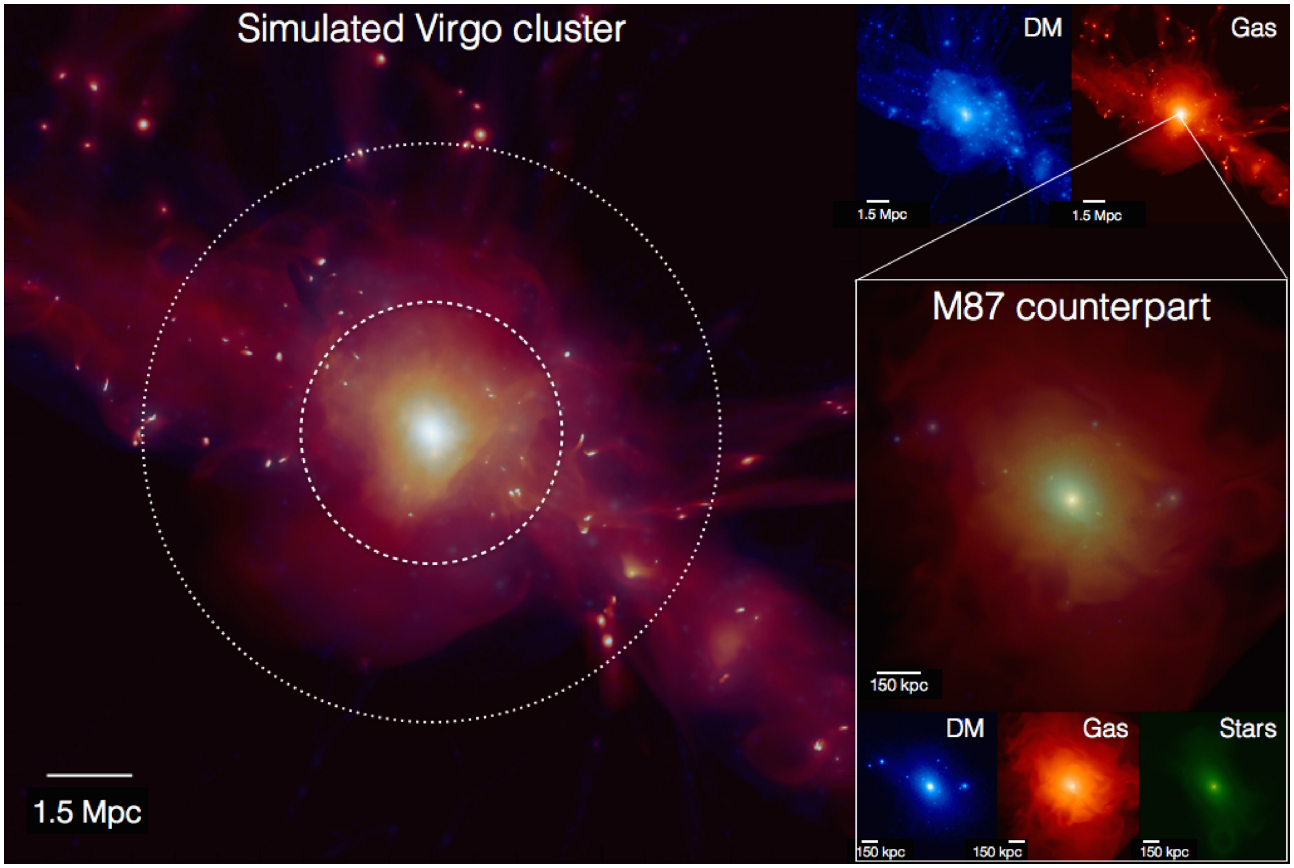

Figure 1. Simulated Virgo cluster of galaxies and its central galaxy M87. The largest panel is a combination of dark matter and gas, shown separately in blue and red in the two top right panels. The second largest panel gathers dark matter, gas, and stars as seen in blue, red, and green, respectively, in the bottom right three panels. The dashed white line delimits the virial radius, while the dotted white line gives the zero velocity radius, i.e. the radius at which the mean radial velocity of galaxies starts to be zero. See the appendix for a more detailed explanation.

distribution at $z = 0$ (see table 1 and 2 of Sorce et al. 2019, for other examples and more details). As a matter of fact, we found that only 30 per cent of the cluster-size random haloes comply within 3σ with the mean values (radius, velocity, number of substructures, spin, velocity dispersion, concentration, centre of mass offset with respect to the spherical centre, *all together*) of our Virgo counterparts at $z = 0$, while 97 per cent of simulated Virgos are in their own 3σ scatter simultaneously for the properties mentioned before, i.e. a simulated Virgo with one property value in the tail of the property distribution is likely to have all its other property values in the distribution tails. Note that the percentage of random haloes in the 3σ scatter drops to 18 per cent when adding the requirement of a similar merging history up to $z = 4$, while that of simulated Virgos stays stable. A study based on a more than 20 000 cluster-size random haloes revealed that the cluster environment is the main driver for such differences (Sorce, Gottlöber & Yepes 2020). Hence, the importance of using a counterpart, i.e. a cluster in a proper large-scale environment, for such studies.

Because they are in their proper large-scale environment, our 200 simulated Virgos thus share similar properties and histories. Still, among our 200 realizations, we had to select one for resimulation. We chose the most representative of the full sample, i.e. the Virgo cluster counterpart that has the properties, mentioned hereabove, the closest to the average properties of the full sample of 200 simulated Virgos and a merging history in agreement with the mean history of the total sample. There is no need to select on any other aspect, such as a particular feature during the formation history, since, by construction, they share a history with the same features.

To avoid periodicity problems in the local Universe-like region, the boxsize of the selected constrained realization is set to ∼740 Mpc at $z = 0$ (Sorce et al. 2016a). To decrease the computational cost of the run and since our interest lays solely in the study of the simulated Virgo cluster in this paper, the zoom-in technique, first proposed by Bertschinger (2001) and implemented in MUSIC (Hahn & Abel 2011), is used with an effective resolution of 8192^3 particles for the highest level (here level 13), corresponding to a dark matter particle mass of $m_{\rm DM,hr} \approx 3 \times 10^7$ M$_\odot$, within a ∼30 Mpc diameter zoom-in region centred on the Virgo cluster counterpart at $z = 0$. Namely, there are more than 35 million dark matter particles within the ∼15 Mpc radius zoom-in region at $z = 0$ that are traced back to the initial redshift. This large zoom-in region is motivated by indications from observations that the environment influences some galaxy properties out to several times the virial radius (e.g. von der Linden et al. 2010; Wetzel, Tinker & Conroy 2012).

2.2 Hydrodynamical features

A full set of key physical processes are included as subgrid models to form a realistic population of galaxies, following the implementation of the Horizon-AGN run (Dubois et al. 2014c, 2016) augmented with BH spin-dependent feedback of active galactic nuclei (AGNs) with no cluster specific calibration:

Radiative gas cooling and heating are modelled assuming photoionization equilibrium within a homogeneous ultraviolet (UV) background. The later is imposed from reionization redshift $z_{\rm reion} = 10$ following Haardt & Madau (1996). The contribution from metals released by supernovae is included in the cooling curve (Sutherland & Dopita 1993) down to $T = 10^4$ K. Various synthesized chemical elements are accounted for but they do not contribute separately to the cooling curve. For simplicity, the tabulated cooling rates rely on the same *relative* abundance of elements as in the sun. The gas follows the equation of state of an ideal monoatomic gas with a 5/3 adiabatic index.

Star formation is allowed wherever the gas density is greater than 0.1 H cm^{-3} with a random Poisson process spawning stellar particles of mass $m_{\rm s,res} = 1.4 \times 10^5$ M$_\odot$ (Rasera & Teyssier 2006) according to a Schmidt law with a constant star formation efficiency of 0.02 (Krumholz & Tan 2007).

Kinetic feedback from type II supernovae is modelled via a modification of the gas mass, momentum, and energy in the surrounding cells (Dubois & Teyssier 2008) assuming a Salpeter-like initial mass function (IMF): release of 10^{51} erg per 10 M$_\odot$ type II supernova with a fraction of the interstellar medium turning into supernovae of $\eta_{\rm SN} = 0.2$. Each individual stellar particle deposits $m_{\rm s,res}\eta_{\rm SN}10^{50}$ erg M$_\odot^{-1}$ at once after 20 Myr with a 0.1 metal yield with respect to its own content.

AGN feedback is modelled assuming that a fraction of the rest-mass accreted energy, prescribed by the capped-at-Eddington Bondy–Hoyle–Littleton accretion rate, on to BH particles, is returned back into the surrounding gas.

A bimodal[1] AGN feedback model is assumed to mimic the quasar-like wind release of (i) a radiatively efficient Shakura & Sunyaev (1973) accretion disc – when the accretion rate is larger than 1 per cent Eddington or (ii) a radiatively inefficient accretion disc, powering collimated jets into their surroundings – when the accretion rate is below 1 per cent Eddington (see Dubois et al. 2012, for technical details of the accretion–ejection scheme).

This BH model tracks not only the mass, but also the spin of the BH that can be modified by binary BH coalescence and gas accretion as detailed in Dubois, Volonteri & Silk (2014a) and Dubois et al. (2014b) for the quasar regime and following the magnetically chocked accretion disc solution from McKinney, Tchekhovskoy & Blandford (2012).

Quasar mode feedback efficiency is set up to $0.15\epsilon_{\rm r}$, where $\epsilon_{\rm r}$ is the Eddington rate, in order to reproduce the BH-to-galaxy mass relation (Dubois et al. 2012). The efficiency of the jet mode feedback is a function of the spin of the BH according to the solution of McKinney et al. (2012; see Dubois et al. 2020, for more details). Note that the radiative efficiency ($\epsilon_{\rm r}$) that intervenes in both the Eddington limit and the quasar mode overall efficiency is a function of the BH spin as well.

BH seeds of 10^5 M$_\odot$ are formed when the gas density is larger than 0.1 H cm^{-3}, the local star density is greater than a third of the local gas density, and there are no existing BH within 50 ckpc (Dubois et al. 2012).

2.3 Run properties

The simulation ran on 5040 cores using about 10 TB of memory from the starting redshift 120 to redshift 0 during 6 million CPU hours with the adaptive mesh refinement RAMSES code (Teyssier 2002) within the Planck cosmology framework with total matter density $\Omega_{\rm m} = 0.307$, dark energy density $\Omega_\Lambda = 0.693$, baryonic density $\Omega_{\rm b} = 0.048$, Hubble constant $H_0 = 67.77$ km s^{-1} Mpc^{-1}, spectral index $n_{\rm s} = 0.961$, and amplitude of the matter power spectrum at 8 h^{-1} Mpc $\sigma_8 = 0.829$ (Planck Collaboration XVI 2014).

The Euler equations are solved with the MUSCL-Hancock method: a second-order Godunov scheme linearly interpolates, with MinMod total variation diminishing scheme, hydrodynamical quantities at cell interface to solve the Euler equations with the approximate Harten-Lax-van Leer-Contact Riemann solver (Toro, Spruce & Speares 1994).

The initial coarse grid is adaptively refined down to a best-achieved cell size of 0.35 kpc roughly constant in proper length. That is, a new level is added at expansion factors $a = 0.1$, 0.2, 0.4, and 0.8, hence, up to level 21 beyond $a = 0.8$. The mesh in the zoomed-in region is allowed to be dynamically refined (or derefined) from level 13 down to level 21 according to a pseudo-Lagrangian criterion: whenever the total density in a cell is larger (smaller) than $\rho_{\rm DM} + (\Omega_{\rm DM}/\Omega_{\rm b})\rho_{\rm b} > 8m_{\rm DM,\,hr}/\Delta x^3$, where $\rho_{\rm DM}$ and $\rho_{\rm b}$ are, respectively, the dark matter (DM) and baryonic mass densities in the cell of size Δx, $\Omega_{\rm DM} = \Omega_{\rm m} - \Omega_{\rm b}$ and $m_{\rm DM,hr}$ is the dark matter particle mass for the highest level. The particle-in-cell technique permits deriving the gravitational potential.

A companion simulation with dark matter only using exactly the same features but for the hydrodynamical part was run. Comparisons between this run and the hydrodynamical run are presented in Appendix A. It shows that the hydrodynamical component did not perturb beyond its normal effect the dark matter halo.

3 SIMULATED VERSUS OBSERVED GALAXY POPULATION

We apply the halo finder algorithm described in Aubert, Pichon & Colombi (2004) and Tweed et al. (2009) to identify galaxies and dark matter haloes in the zoom-in region. In this algorithm, haloes (galaxies) are detected in real space using the local maxima of the density field obtained with dark matter (star) particles. More precisely, haloes (galaxies) are detected in real space using the local maxima of the density field obtained with dark matter (star) particles. Their edge is defined as the point where the overdensity of dark matter (stellar) mass drops below 80 times the background density. We further apply a lower threshold of a minimum of 100 dark matter (50 star) particles. The particle content of our objects is further 'exclusive', i.e. particles belonging to substructures have been removed. That approach allows us to unambiguously investigate the intracluster stellar component. Merger trees permit following galaxies and their evolution across cosmic time, in particular when they cross paths with the cluster. We analysed 110 snapshots between $z = 0$ and $z = 7$. Then, for each galaxy, we derive the following properties:

(i) We define the entering time in the cluster as the time when a galaxy crosses the cluster virial radius at time t for the first time. The later is found via the virial theorem. The later must be verified at a 20 per cent precision. The specific study of backsplash galaxies at $z = 0$, namely galaxies that entered the cluster recently but exited and did not enter again at $z = 0$, is postponed to a future paper. For information, they represent 5 per cent of our total galaxy sample, i.e. in a ∼12 Mpc radius spherical volume. If they were to be in the cluster virial radius at $z = 0$, the actual number of galaxy within the cluster would be increased by 26 per cent.

[1]Thermal or kinetic depending on the accretion efficiency.

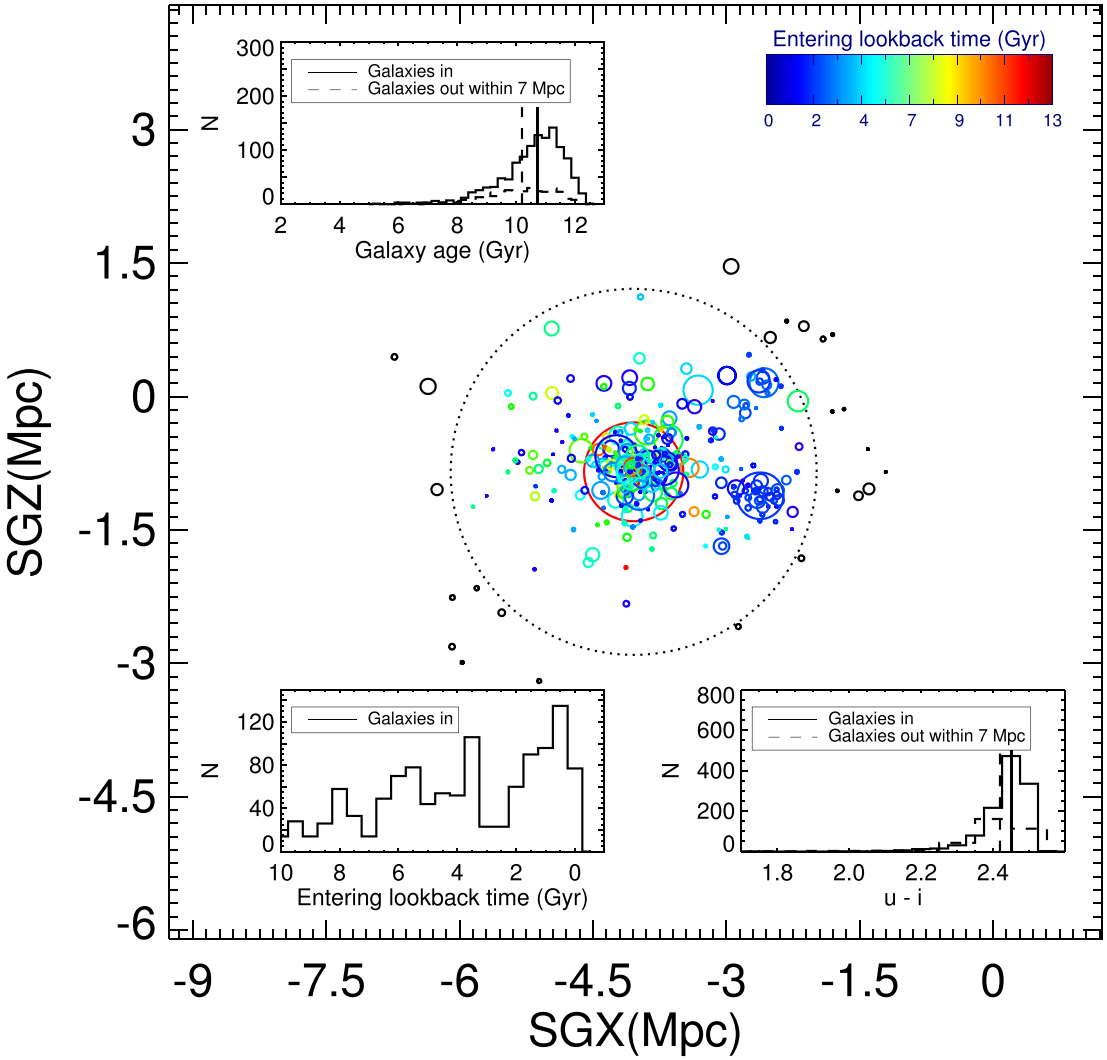

Figure 2. Main: Simulated galaxies in the Virgo cluster counterpart (i.e. within its ∼2 Mpc virial radius) and up to ∼3 Mpc from its centre, in a tenth of its virial radius (∼0.2 Mpc) thick slice. The dotted circle stands for the virial radius of the simulated dark matter halo at $z = 0$. Coloured solid circles represent galaxies. Diameters are proportional to the virial radius of galaxies. Galaxies represented by redder (bluer) circles entered earlier (later) in the cluster counterpart. Galaxies that are not within the virial radius of the cluster at $z = 0$ are in black. Top left and bottom right insets: galaxy age and colour distributions inside and outside the virial radius of the cluster as well as their medians. Bottom left inset: galaxy entering time in the virial radius of the cluster. Coordinates are supergalactic coordinates of the Virgo cluster counterpart. Galaxies within the cluster are in general older and redder.

(ii) Magnitudes and rest-frame colours of galaxies are derived using single stellar population models from Bruzual & Charlot (2003) and a Salpeter IMF in agreement with the hydrodynamical model we use in the simulation: each star particle contributes to a flux per frequency that depends on its mass, metallicity, and age. The contribution of all stars is then summed and filtered to obtain the flux in different bands. Then total luminosities or magnitudes are derived. Since the Virgo cluster is nearby, rest-frame quantities are valid. In this work, attenuation by dust is not included. This implies that observed galaxies have to be corrected for dust extinction before any comparisons with the simulated galaxies. Future work will look in more detail at the dust extinction effect.

(iii) Three star formation rates (SFRs) are derived: the amount of stars formed over 10, 100, and 1000 Myr. Depending on the study at in question, they will be used alternatively to compare with observations. The specific star formation rate (sSFR) is the ratio of the SFR to the current galaxy stellar mass. Note that there is no distinction between stars formed *in situ* and those formed *ex situ* that have been accreted. The ratio of *in situ*/*ex situ* stars is a vast topic of research in itself and thus is postponed to future studies.

(iv) Galaxy metallicity and age are obtained with a sum over all the star particles belonging to the galaxy weighted by their mass.

On a qualitative aspect, Fig. 1 shows the simulated Virgo cluster as well as its central galaxy M87, today. Their dark matter is in blue, while the red colour stands for their gas. The stellar density of M87 counterpart is in green. On a more quantitative aspect, Fig. 2 shows a static view of the galaxies in the cluster today in a slice of a tenth of its virial radius. The dashed black line stands for its virial radius and the circles represent galaxies with sizes proportional to their virial radii. The gradient of colour from blue to red gives the entering time in the cluster with galaxies that entered earlier in red. The black colour stands for galaxies up to 3 Mpc from the cluster centre, but not within the virial radius of the cluster at $z = 0$. As expected, galaxies that entered earlier on are in the cluster core.

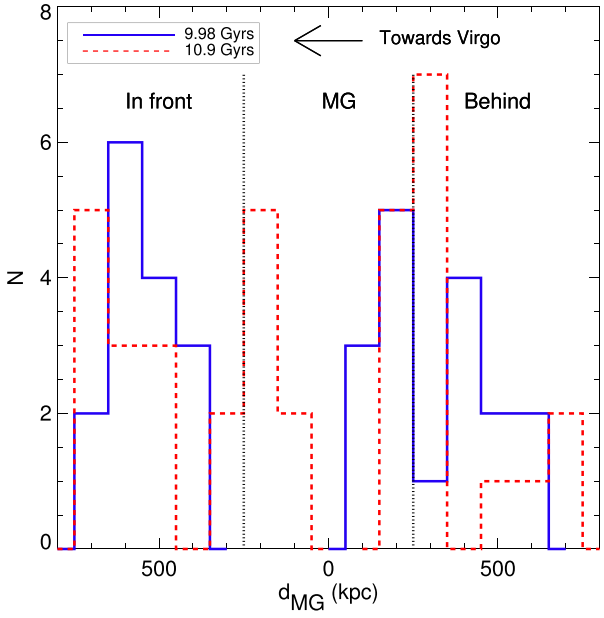

Figure 3. Galaxy distributions around the most massive galaxy (MG) of the infalling group when the Universe was about 10 Gyr (blue solid histogram) and 11 Gyr (red dashed histogram) old. Galaxies within the Virgo cluster counterpart radius at these given times are excluded. The virial radius of the dark matter halo host of the group MG is about 250 kpc (dotted black lines). The number of galaxies within this main halo ($d_{\rm MG} < r_{\rm vir}$) increased during that time period. Galaxies are split between those behind this halo with respect to the Virgo cluster counterpart and those between the halo and Virgo counterpart. Clearly, during that time period, galaxies tend to accumulate around MG. The infalling group thus congested during that time period the filament preventing galaxies from falling on to the Virgo cluster counterpart until it finally fell itself.

Three small insets give the galaxy age, entering time, and colour distributions with medians for galaxies inside and outside of the cluster. As expected, galaxies in the cluster virial radius are on average redder and older than those outside. There is a significant gap in galaxy accretion about 3 Gyr ago spanning over 1 Gyr. Interestingly, it appears just before the beginning of the last significant merger mentioned in the introduction and discussed hereafter. It seems like the infalling group congested during a while the main filament channelling matter into the cluster, hence preventing the accretion on to Virgo counterpart of any other small isolated galaxies for a while. Note that such a preferred direction of infall into the cluster alongside a main filament is observationally confirmed (West & Blakeslee 2000). More precisely, Fig. 3 shows that the group grew over that period of time, accreting around its most massive galaxy the smaller galaxies that were channelled to the filament. Filaments are indeed known to be the main drivers of matter into the clusters (Umehata et al. 2019). On this figure, the galaxy distribution around the main galaxy (MG) of the group varies within that time period. Note that galaxies already within the Virgo cluster counterpart at the given time are excluded. First, the number of galaxies within the virial radius of the dark matter halo host of the MG ($d_{MG} < 250$ kpc) grows (solid blue versus dashed red line histograms in between the two dotted black lines). Second, always within that time period, galaxies that are behind the group with respect to the Virgo cluster counterpart tend to accumulate at the edge of the dark matter halo virial radius. Third, galaxies between the group and the Virgo cluster counterpart either are accreted on to the simulated cluster or retained by the small group creating a small dip in the galaxy distribution. Hence, fewer galaxies entered within the simulated cluster until the small group itself went in. There is another, although less significant, decrease in galaxy accretion about 7 Gyr ago. It corresponds to the typical transition for a Virgo-like simulated cluster between an active period of mass accretion, relative to an average random halo, and a quiet history (see Sorce et al. 2020, for a detailed explanation).

3.1 Simulated versus observed general distributions

Velocities and distances in the observed and numerical cluster-centric systems are derived with the formula and geometric considerations given by Karachentsev & Kashibadze (2006; see Appendix B for details). Fig. 4 shows the distribution of the velocities as a function of the distance to the cluster centre for the observed cluster and for the simulated cluster without and with errors on distances. Because the observed galaxy sample does not fulfill any specific completeness, i.e. the only requirement is to have both a direct distance measurement of the galaxy and its redshift, simulated galaxies are simply randomly selected to match the number of galaxies in the observational sample and facilitate the comparisons with the observed cluster. Additionally, in the third panel of the figure, errors up to 20 per cent have been added to distances to mimic direct distance measurement uncertainties (e.g. Tully, Courtois & Sorce 2016). Redshift uncertainties are negligible in this case. Running medians, derived with a window of 1.5 Mpc, are plotted on top of the Hubble diagrams as solid orange lines. The dot–dashed blue line is the Hubble law with $H_0 = 67.77$ km s^{-1} Mpc^{-1}. The dotted violet and orange lines indicate the virial and zero velocity radii (see Appendix C for the definition of the latter radius). The similarities between the observed and simulated Virgo clusters are remarkable. Actually, the only clear difference between the left-hand and middle panels is in the intrinsic scatter around the Hubble law at large cluster centric distances. This scatter appears larger in the observational case than in the simulation case. It is exclusively due to distance estimate uncertainties in observations that propagate to velocities and that are absent in the simulation as shown by the right-hand panel.

Peng et al. (2008) derived the *V*-band magnitude, the distance to the cluster centre, and the stellar mass of a subsample of galaxies in the Virgo cluster. Stellar masses are obtained combining the $(g - z)$ and $(J - K_s)$ colours to simple stellar populations modelling with a Chabrier IMF to get mean mass-to-light ratios in z band. Fig. 5 (left) shows as a solid blue line the average magnitude by distance bin for this subsample of early galaxies ($g - z > 1.2$; Ferrarese et al. 2006) with SDSS *B*-band magnitudes smaller than -15.11. In addition, their sample is only complete at the brightest end (-19.1 in SDSS *B* band). Ultimately, they reach only 44 per cent completeness in the sample probed here (Côté et al. 2004). The error bars are the standard deviations. The blue circle is M87. The dotted black line stands for the simulated galaxies. To legitimize the comparison, the simulated sample is cut to match the observational restriction: $g - z > 1.2$, magnitude larger smaller than -15.11 in the *B* band and 44 per cent completeness above -19.1 *B*-band magnitude. Since they claim to have a homogeneous representative subsample, we select randomly 44 per cent of the galaxies for *B*-band magnitude above -19.1. The dashed red line shows the result. The filled red circle is the counterpart of M87 that happens to be brighter than the observed one. In the latter case, it is important to note, however, that luminosity asymptotes are not reached before 100–300 kpc for massive central galaxies like M87 (Kravtsov, Vikhlinin & Meshcheryakov 2018). As a consequence, its total magnitude is underestimated. Subsequently, the simulated M87 appears too massive (right-hand panel of the figure). A small aperture indeed leads to an underestimated stellar mass by at least a factor 2–4

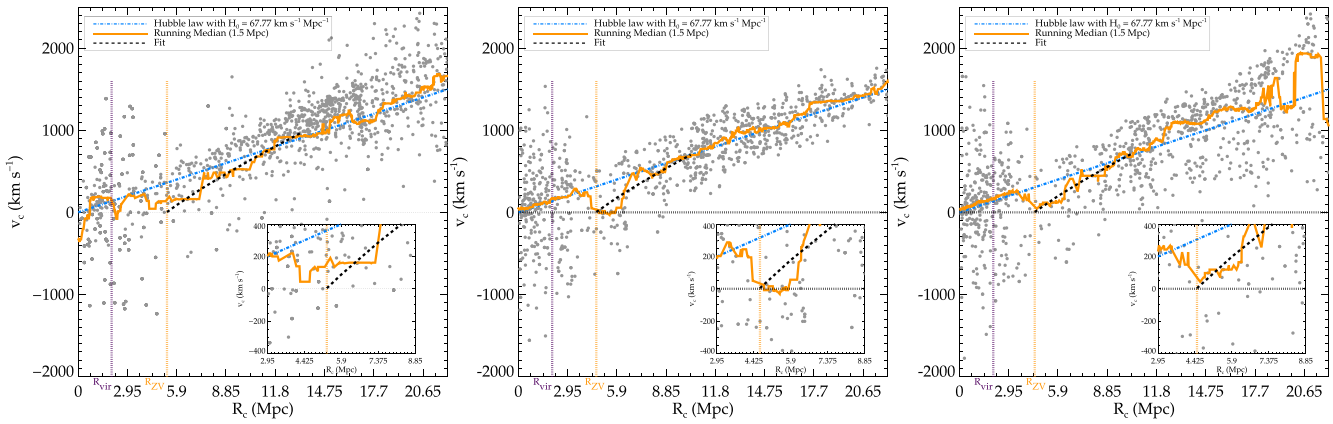

Figure 4. Observed data from Tully et al. (2008) (left) and simulated, without (middle) and with (right) error on distances, galaxy velocities with respect to the centre of the observed and simulated Virgo cluster. Dotted violet and yellow lines stand for the virial and zero velocity radii. The dot–dashed blue line is the Hubble flow while the dashed black line is a fit to the running median shown with a orange solid line. The small insets are zooms on the zero velocity radius. Only a fraction of the simulated galaxies have been randomly selected to reproduce the same number of galaxies as in the observed sample to properly draw comparisons and estimates of the zero-velocity radius. The dynamical distributions of galaxies in the observed and simulated clusters are extremely similar.

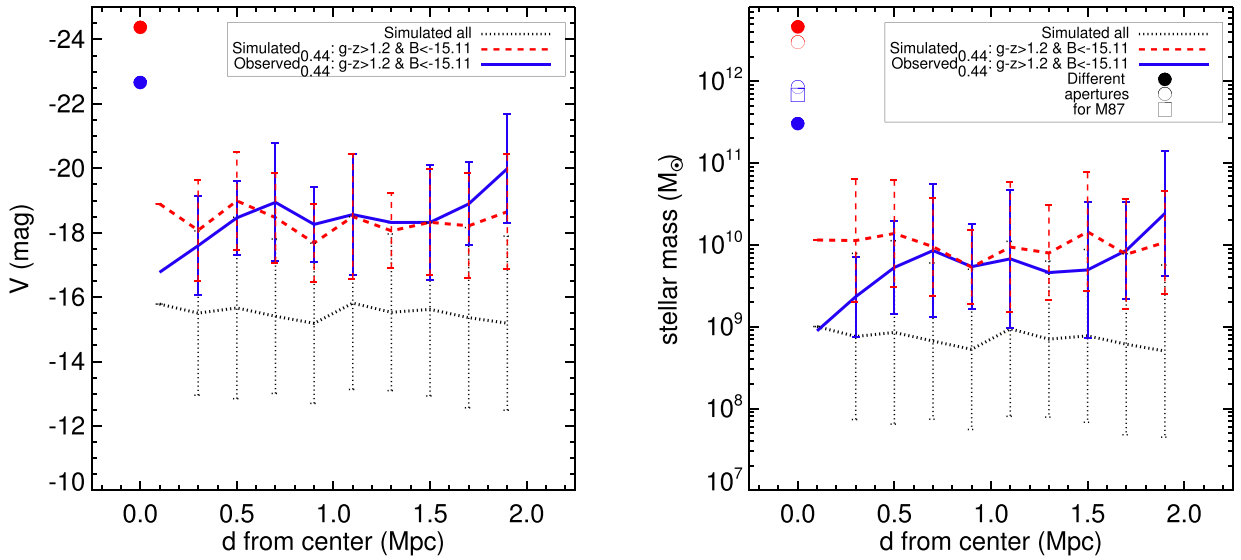

Figure 5. Mean magnitudes (left) and stellar masses (right) of simulated and observed from Peng et al. (2008) galaxies as a function of the distance from the cluster centre. The filled circles stand for the observed (blue) and simulated (red) M87. Open symbols stand for stellar mass estimates of the observed (blue) and simulated (red) M87 in different aperture radii as follows: the open circle is a measure within a ∼148 kpc radius from Gebhardt & Thomas (2009) and the open square gives the measurements within a ∼80.4 kpc radius from Forte, Vega & Faifer (2012) against a ∼5.4 kpc radius for that of Peng et al. (2008). The dotted black lines represent the full sample of simulated galaxies while the dashed red lines are obtained with the sample restricted according to the same requirements as the observed one. The error bars are standard deviations around the mean. Note that there is no statistics in the observed inner core, most probably because galaxies therein are in the shadow of M87 and thus were not selected by the observers. The magnitude and mass distributions of galaxies within the observed and simulated clusters present the same trend. The counterpart of M87 is slightly brighter, thus slightly more massive than the observed M87 by a factor ∼3 when compared to the same aperture radius (open circles).

(Kravtsov et al. 2018). In the following, a more detailed comparison between M87 and its counterpart investigates more closely the difference. Open blue symbols that give mass estimates in larger aperture radii (Gebhardt & Thomas 2009; Forte et al. 2012) already give a hint of a comparison. The open red circle gives the simulated stellar mass in a similar aperture radius as that of Gebhardt & Thomas (2009) (open blue circle).

Coming back to the curves in Fig. 5, the agreement between observationally and numerically obtained curves and their standard deviations is quite remarkable especially because of the approximate match between the observational and simulated samples. The main difference between the observation and the simulation can be found in the cluster core and at the edges of the sampled volume. Close to the centre, there are a few small simulated galaxies while in the observational sample as is, there is no statistics. It could be that the bright M87 makes it challenging to observe small galaxies close to the cluster core. Consequently, in their selection, Peng et al. (2008) did not retain them. Note that the agreement is as impressive between the *V*-band magnitude curves as for the stellar mass curves although they used a Chabrier IMF to derive stellar masses while we used a Salpeter IMF

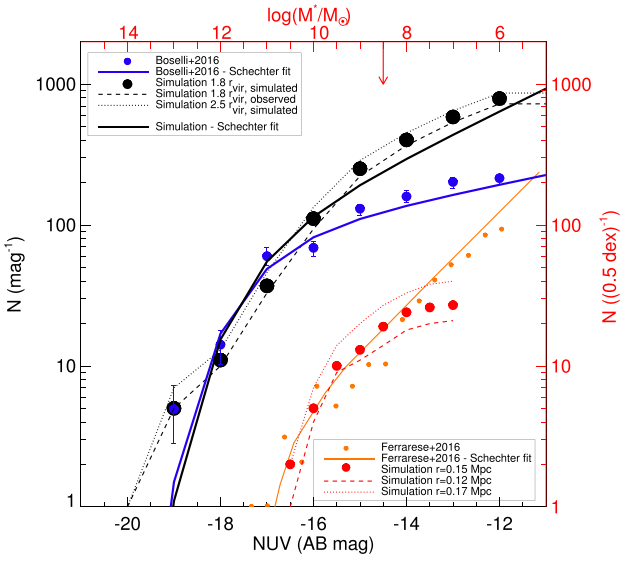

Figure 6. NUV–luminosity (cold colours) and stellar mass (warm colours) functions of the observed (blue and orange, respectively, from Boselli et al. 2016a; Ferrarese et al. 2016) and simulated (black and red, respectively) Virgo clusters. Different search radii are used in the simulation: filled circles, dashed and dotted lines. Schechter fits are shown as solid lines. The red arrow indicates the stellar mass resolution limit of the simulation. In both cases, the simulated function matches relatively well the observational estimates at the brightness/most massive end. The agreement is excellent all the way down to the resolution limit for the stellar mass function.

to reversely derive magnitudes. At the observational sample edges, the completeness is most probably affected by distance uncertainties that are about 0.5 Mpc. Still overall the agreement is quite good.

To push deeper the comparison, it is necessary to refer to the luminosity and stellar mass functions of the Virgo cluster that are obtained with complete (or corrected for completeness) samples. Fig. 6 reports two of these most recent functions (Boselli et al. 2016a; Ferrarese et al. 2016) within different radii: about 0.15 and 2.88 Mpc ($1.8 \times r_{\rm vir\,observed}$). The agreement with their simulated counterparts is remarkable. For the stellar mass function, the observational Schechter fit shown as a solid orange line matches perfectly the simulation (red filled circles) down to the mass resolution limit (red arrow and see Appendix D). As for the luminosity function, identical Schechter functions but for the α slope characterizing the faint end can be used:

$$\phi(M) = (0.4\ln10)\phi^*[10^{0.4(M^*-M)}]^{(1+\alpha)}\exp[-10^{0.4(M^*-M)}], \quad (1)$$

where M is the absolute magnitude, and α, ϕ^*, and M* are the fitting parameters. α is slightly larger (-1.4 against -1.19) in the simulation than in the observations. Two parameters might come into play: (1) we used a Salpeter IMF to derive retroactively the near-UV (NUV) band magnitude that could give lower (in absolute value) magnitude, shifting galaxies from higher magnitude bins to lower ones and (2) the feedback is not efficient enough at suppressing star formation in the intermediate-mass galaxies. An on-going run with a Kroupa IMF based feedback will permit evaluating both of these effects.

In future studies of Virgo counterpart substructures, we will go into more detailed comparisons between their observed and simulated luminosity functions as proposed by Boselli et al. (2016a). Before moving to the next subsection, we stress again the excellent agreement between the simulated and observed functions.

3.2 Simulated versus observed M87

The simulated cluster reproduces overall the spatial and luminosity distribution of observed galaxies within the Virgo cluster. It is worth pushing further the comparison for M87, its central galaxy.

Fig. 7 gives the formation and evolution of M87 counterpart's properties (lines) as well as observational estimates nowadays (filled circles and dotted blue line). Colour estimates are from SDSS (Adelman-McCarthy et al. 2009) and GUViCS (Gil de Paz et al. 2007), the stellar mass is from Gebhardt & Thomas (2009), and the average metallicity and age are from Liu et al. (2005):

(i) Stellar mass: as mentioned in the previous subsection, bright cluster galaxies usually have stellar masses underestimated by a factor 2–4 because their cumulative stellar mass continues growing at the last measured aperture radius. Fig. 8 (left) shows the cumulative stellar mass profile for M87 (Gebhardt & Thomas 2009) and its counterpart as well as stellar masses from Peng et al. (2008) and Forte et al. (2012). Clearly, the latter are lower limits. It confirms that the discrepancy observed between filled red and blue circles in Fig. 5 is mostly due to the aperture. The estimate from Gebhardt & Thomas (2009) is closer to the total stellar mass of M87 but is still on the low side. The asymptotic value is not yet completely reached. This effect combined with residual extinction in the observation and a lack of feedback mitigating star formation in the simulation could explain the residual difference. The BH in the simulated M87 might start growing too late, thus its feedback happens too late.

(ii) Age: the SFR peak (both *in situ* and *ex situ* stars) of the simulated M87 and the mean age of stars in the observed M87 are a close match. The second panel in Fig. 8 confirms that simulated and observational ages are similar especially since observational estimates are measured within less than 40 kpc.

(iii) Metallicity: observed and simulated metallicities of M87 are really close. However, Fig. 8 shows that, because of the same small aperture radius (40 kpc) used to measure the metallicity, there is in fact a discrepancy and they cannot be considered identical. In a third paper, we will show that the simulated hot gas has a too low metallicity with respect to the observed one, an explanation can be partly found here: metals are insufficiently released by stars.

(iv) Colours: the discrepancy is the most import for the ($u - i$) colour. However, the SDSS u-band might not be the best at measuring luminosity of Brightest cluster galaxies (BCGs). Indeed it has a higher systematic uncertainty (Padmanabhan et al. 2008), it is more susceptible to dust extinction, and it is nearer to the unexplained UV upturn that appears in elliptical galaxies (Loubser & Sánchez-Blázquez 2011). The discrepancy is somehow of a lesser extent for other colours such as ($g - i$) and ($B - V$). In these cases, a small residual extinction in observations might explain part of the difference. A lack of feedback dampening star formation in the simulation could also perhaps explain the bluer colour for the simulated M87 than the observed one. However, removing the youngest stars in the simulated galaxy does not drastically change its colour (by $+0.01$ at most with the minimum age at 10 Gyr). In addition, the simulated colour profile shown in Fig. 8 shows that there is no drastic change with the aperture radius either and in any case it makes the simulated galaxy even slightly bluer (by about -0.01).

Besides M87 associated with the cluster A (Boselli et al. 2014), the Virgo cluster hosts other old massive galaxies like M60 (cluster C) and M49 (cluster B) with respective mass estimates of roughly about 10^{12} and 5×10^{11} M$_\odot$ at distances of 0.4 and 0.6 Mpc from M87 with ($g - i$) colour of 1.34 and 1.30 mag (values obtained with SIMBAD queries at CDS). A quick look in the simulation reveals two old

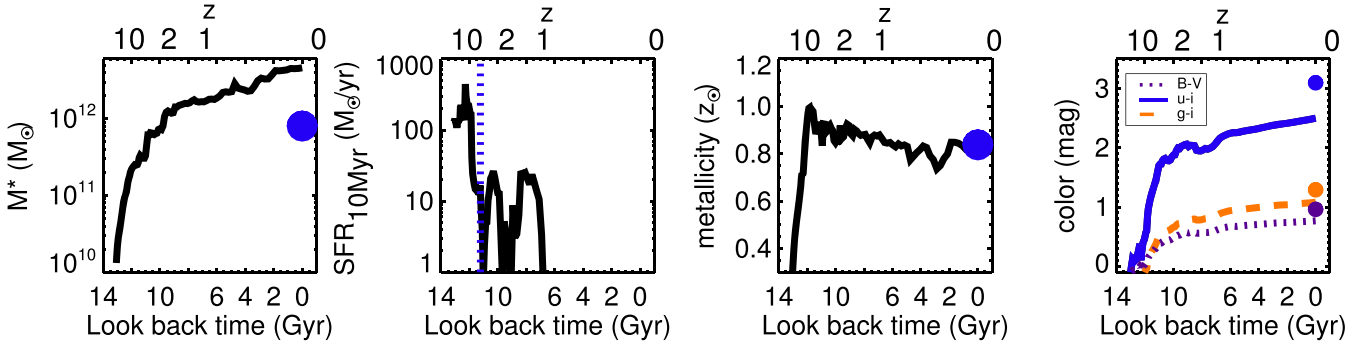

Figure 7. Evolution history of the properties of M87 counterpart. Filled blue, orange, and violet circles stand for the observational estimates of M87 today: stellar mass from Gebhardt & Thomas (2009), average metallicity and age from Liu et al. (2005), and colours from SDSS (Adelman-McCarthy et al. 2009) and GUViCS (Gil de Paz et al. 2007). The dotted blue line in the second panel stands for the average age of observed stars at the centre of M87. Solid lines in each panel as well as the dotted and dashed lines in the last panel are values for the simulated M87 across cosmic time. While the mean age of stars in the counterpart of M87 and its mean metallicity match observational estimates, M87 is redder and less massive than the simulated one.

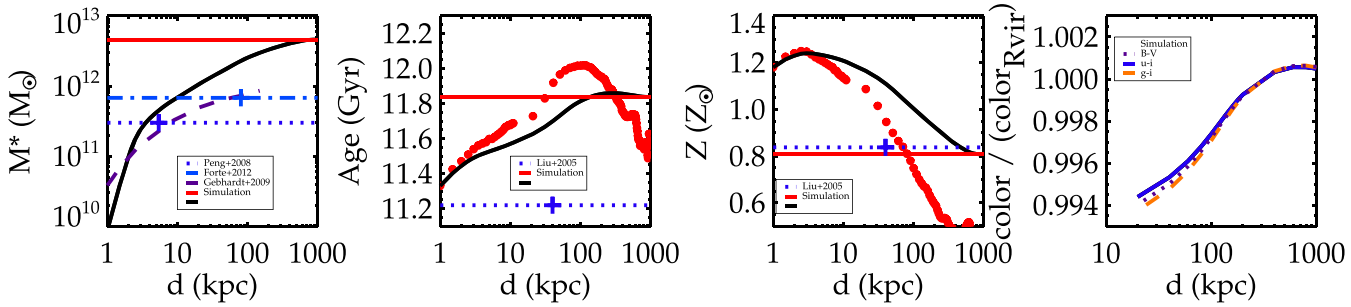

Figure 8. From left to right: Solid black lines are stellar mass, age, and metallicity cumulative profiles of M87 counterpart. Lines in the last panel stand for the ratio of colours within a given aperture radius (d) to that within the virial radius of the simulated galaxy. Blue lines (but in the last panel) are observational estimates for a given aperture radius marked as a blue cross: stellar mass from Peng et al. (2008), Forte et al. (2012), and Gebhardt & Thomas (2009) with respective aperture radii of 5.4, 80.4, and 148 kpc, average metallicity and age from Liu et al. (2005) using a 40 kpc aperture radius. The violet line in the left-hand panel is the cumulative stellar mass estimate profile of M87. Straight red lines stand for global simulated values for M87 counterpart within its virial radius. Filled red circles give estimates per bin of galactocentric distances. Aperture radii explain part of the discrepancy between the observational and simulated mass and age estimates of M87, but not that between metallicity and colour estimates.

galaxies (11.1 and 11.3 Gyr) of masses 6×10^{11} and $3.5 \times 10^{11} M_{\odot}$ at 0.3 and 0.4 Mpc from M87 counterpart with $(g - i)$ colour of 1.06 and 1.05 mag. Without being close matches to M60 and M49, their presence is interesting and further studies with their associated large substructures (Boselli et al. 2014) within the simulated Virgo cluster will be the subject of a future paper. Note that the shift in colours is found again and seems systematic. Simulated old massive galaxies appear definitively bluer than their counterparts, comforting the too low AGN feedback hypothesis.

4 FORMATION HISTORY: FROM OBSERVATIONALLY DRIVEN TO NUMERICALLY CONFIRMED FORMATION SCENARIOS

4.1 Accretion rate of galaxies

The overall good agreement between observations of the Virgo cluster and the simulated one allows us to further compare the observationally derived formation scenarios and the numerical findings.

Boselli et al. (2008) deduced from observations that about 300 galaxies with stellar mass above 10^7 $M_{\odot}$ should have entered the cluster each Gyr within the last few Gyr. From observing that a large amount of small galaxies are quickly turning red in the inner cluster, Boselli & Gavazzi (2014) even concluded that most of them should have entered within the last 500 Myr (Boselli et al. 2016b). According to Fig. 9, 279 galaxies with stellar masses between 10^7 and 10^{11} $M_{\odot}$ entered the cluster within the last Gyr. Correcting for completeness (see Appendix D), it means that between 280 and 330 simulated galaxies with masses ranging from 10^7 to 10^{11} $M_{\odot}$ entered the cluster within the past Gyr (depending on when the galaxies – missing within the virial radius of the simulated cluster because of the lack of completeness at these masses – entered the cluster). It is also clear that lately, the simulated Virgo cluster did not accrete major galaxy groups but mostly isolated small galaxies as already shown in our previous studies but based on dark matter-only simulations (e.g. Olchanski & Sorce 2018). Additionally, the figure confirms that a lot of these small galaxies entered the cluster recently with a maximum within the last 500 Myr just like the observationally deduced.

To summarize, this paper confirms that results obtained within a series of paper based on dark matter-only simulations of the Virgo cluster are not affected by the inclusion of baryons and it also goes further. In agreement with observations:

(i) the simulated Virgo cluster has had a quiet merging history within the last few Gyr while it used to grow faster (see Sorce et al. 2019, for the DM study),

(ii) about 300 small isolated galaxies entered recently in the cluster, most of them within the last 500 Myr.

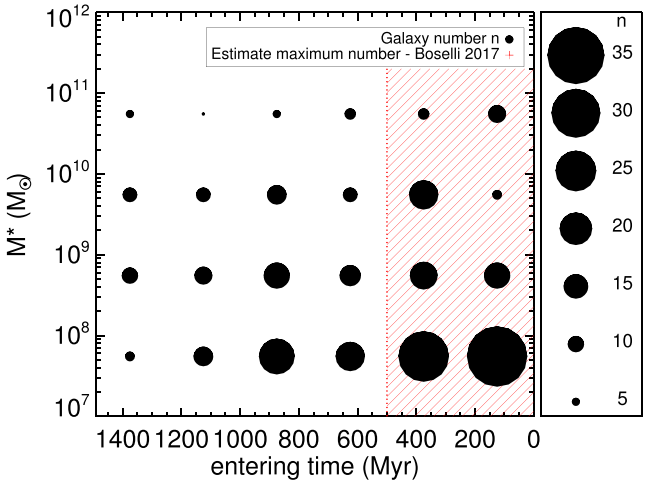

Figure 9. Number of galaxies per today mass bin and per 250 Myr that entered the cluster. Sizes of filled black circles are proportional to that number. The dashed area stands for the period of time within the last few Gyr when there should be a maximum number of small galaxies entering the cluster according to observations (Boselli et al. 2008). About 300 small galaxies entered the simulated cluster lately mostly within the last 500 Myr in agreement with observationally driven scenarios.

(iii) Virgo counterpart accretes along a preferential direction: the line-of-sight filament (see Sorce et al. 2016b, for the DM study),

(iv) it underwent its last significant merger within the last 4 Gyr,

(v) this merging event finished a bit more than a Gyr ago,

(vi) it was about 10 per cent the mass of the cluster today (for these last three points, see Olchanski & Sorce 2018, for the DM study).

It is interesting to further look at this last merging event.

4.2 The last significant merger

Recently, Lisker et al. (2018) found evidence in their observations of the Virgo cluster that, indeed, a group of about 10 per cent the mass of the cluster probably fell on to it within the last 2–3 Gyr. If it did fall, this group did so along the line of sight, namely it entered the cluster directly on the opposite side from ours. Such a scenario would explain the clustering of quenched galaxies, with high velocities with respect to the cluster centre velocity that are not within the inner core of the cluster in a phase-space diagram. Fig. 2 shows the supergalactic *XZ* plane that permits making visible the simulated last significant merger of about 10 per cent the mass of the cluster today at about (−3, −1.5) Mpc and Fig. 3 shows the gathering of this group. This group happens to have fallen into the cluster through the filament opposite to the centre of the box with respect to the simulated Virgo cluster, namely quasi in the line of sight of an observer close to the centre of the box (where the Milky Way would be), in excellent agreement with the observationally deduced merging history of this group.

More precisely, Fig. 10 (left) reproduces with the simulated galaxies the study conducted by Lisker et al. (2018) with observational data. Positioning an observer directly in the line of sight of the fallen-in group with respect to the cluster, radial velocity in the heliocentric frame of reference [see equation 2 for a conversion from the Cosmic microwave background (CMB) frame of reference] relative to the mean velocity of the cluster in the heliocentric frame of reference as a function of the distance to the centre are derived for the galaxies. Circles represent red galaxies ($g - z > 1.2$). Galaxies are selected in an r-band magnitude range [−19,−18]. Fully filled circles indicate galaxies that belong to the group of ∼10 per cent the cluster mass that fell into the cluster within the last few Gyr in perfect alignment with the cluster and the observer. Conversion from the CMB frame of the reference to the heliocentric one:

$$v_{\rm CMB} = v_{\rm helio} + v_{\rm apex}(\sin(b)\sin(b_{\rm apex}) + \cos(b)\cos(b_{\rm apex})\cos(l - l_{\rm apex})), \quad (2)$$

where $v_{\rm apex} = 371$ km s^{-1}, $b_{\rm apex} = 48.26$ deg, and $l_{\rm apex} = 264.14$ deg from Fixsen et al. (1996), and l and b are galactic coordinates.

Comparisons with the phase-space diagram in fig. 4, second row, of Lisker et al. (2018) and reproduced in the right-hand panel of Fig. 10 lead to exceptional similarities. The group members are found at about the same position as the proposed fallen-in galaxy group in the observational data. Note that the magnitude bin is lower by one unit in the simulated case because of the opposite trend in the red than in the blue case of the Salpeter IMF choice to derive reversely r-band magnitudes from stellar masses. In our case, it gives higher (in absolute value) magnitudes for the same given stellar mass.

One may notice that relative velocities obtained by Lisker et al. (2018) are somewhat smaller than simulation-based relative velocities. Tests changing the line of sight in the simulation show that this shift is probably due to the non-perfect observer – M87–MG alignment in the observation. For instance, a simulated alignment observer – M87–2/3 of the MG-M60 vector as shown in the middle panel permits recovering velocities of the same order as that of Lisker et al. (2018).

In both cases (perfect and non-exact alignments), two simulated galaxies appear close to those belonging to the group in the phase-space diagram (filled diamond and square). The galaxy represented by a filled square fell just before the group. The other galaxy, shown as a filled diamond, followed the group's footsteps but in complete isolation from the latter. Interestingly, it appears to be a backsplash galaxy. This is not at odds with observations since galaxies within this region in the phase-space diagram are only plausible, but not guaranteed, members of the fallen-in group. Note that this latter galaxy is one of the galaxies that are represented at 700 kpc behind the MG of the group in the histogram of Fig. 3.

Finally, Fig. 11 summarizes the accretion history of the Virgo cluster as would be seen by an observer at the centre of the box (where the Milky Way would be). Similarly to what we observe today, lately the accretion happens to be along a preferential direction of infall (filament in the line of sight: galaxies that fell in lately appear to be mostly localized behind the Virgo cluster counterpart represented by a dashed line), quieter than it used to be, with the last significant merger of about 10 per cent the mass of the cluster that started about 2 Gyr ago while very recently only about 300 galaxies per Gyr entered the cluster. Each small inset shows the galaxies that are in the cluster today at an anterior time, namely before they enter the cluster. They are not displayed after they entered the cluster. The thick dashed black line stands for the virial radius at a given time in angular coordinates. The factor used to derive the angular diameter of the cluster given its distance today is also used for earlier redshifts, in other words the angular size is always computed from the same distance that at $z = 0$. The violet color stands for isolated galaxies before entering the cluster, while the light blue colour means that a galaxy is a satellite within a group before entering the cluster. The red colour highlights the galaxies that belong to the last significant merging group.

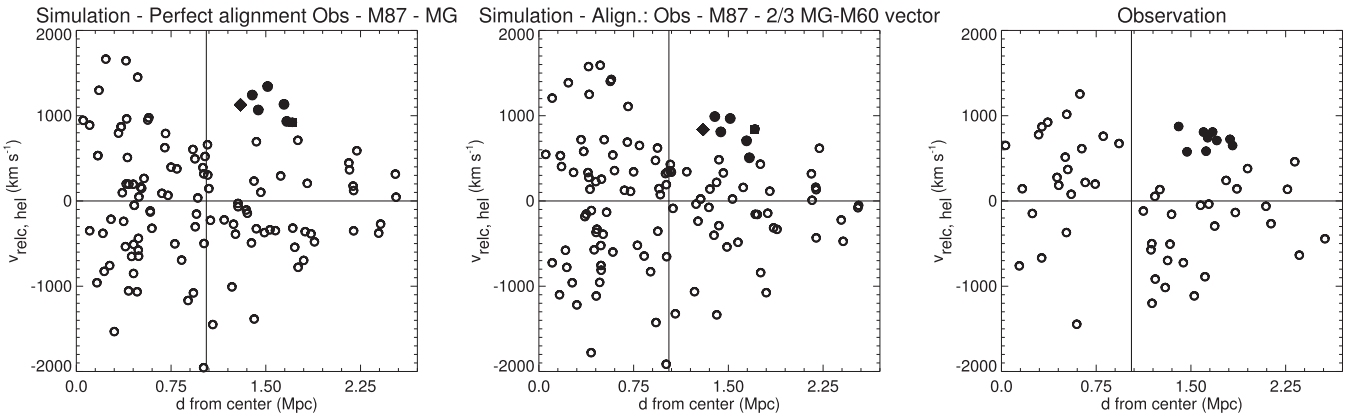

Figure 10. Galaxy velocity with respect to the cluster centre velocity as a function of the distance to the centre for the simulated (left and middle) and observed (right, from Lisker et al. 2018) clusters derived in the heliocentric frame of reference. Left: Circles are simulated galaxies with (g-z) > 1.2. Fully filled black circles denote galaxies that belonged to the group of about 10 per cent the mass of the cluster that merged within the last few Gyr. The MG of the group is taken to be exactly aligned with respect to M87 counterpart and the observer to derive relative velocities. Middle: same as left-hand panel, but the observer is taken to be aligned with M87 and 2/3 of the MG-M60 vector. In these two left-hand panels, the filled diamond stands for a galaxy that fell into the cluster after the group, the filled square represents a galaxy that fell into the cluster before the group. Right: data points from the right-hand panel of fig. 4 in Lisker et al. 2018. Circles are early-type galaxies in the observed Virgo cluster. Filled black circles are potential galaxy candidates that used to belong to a group that merged within the cluster a few Gyr ago. The observational scenario of the merged group somewhat quasi along the line of sight seems confirmed.

5 CONCLUSION

The Virgo cluster of galaxies is our closest cluster neighbour. As such, it is a formidable object of study to understand cluster formation and the evolution of galaxies once they enter this rich environment. To that end, simulations of galaxy clusters are compared to observations of the Virgo cluster. The difficulty rises when observational probes depend on the formation history of the observed cluster. The diversity of clusters makes the one-to-one comparison with numerical simulations a daunting task to disentangle nurture versus nature. To remove the nurture from the study and focus only on the nature, it is necessary to produce a numerical cluster within the proper environment. Only then the tool is optimal to study the great physics laboratory that is the Virgo cluster.

The goal of this first paper of a series is to present the first full zoom-in hydrodynamical simulation of a counterpart of the Virgo cluster of galaxies, a CLONE simulation of Virgo, that has been obtained by constraining initial conditions with only local galaxy radial peculiar velocities. The large-scale environment of the cluster resembles our local neighbourhood. The zoom-in region has a $\sim$15 Mpc radius with an effective number of 8192^3 particles for the highest level (particle mass of $\sim 3 \times 10^7$ M$_\odot$) and a refinement down to 0.35 kpc. AGN and supernova feedbacks are included. This paper confirms that overall the simulated cluster reproduces the observed cluster well enough for future deeper comparisons of galaxy population and hot gas phase in the inner core.

First, general comparisons between the observed galaxy population of the Virgo cluster and the simulated one reveal excellent agreements in terms of luminosity and mass distribution as a function of the cluster centre. A focused comparison between M87 and its simulated counterpart confirms the similarities. M87 counterpart is perhaps a bit too massive but some of this mass might be due to residual extinction in the observation and most probably a slightly too weak feedback in the simulation.

Observationally driven formation and evolution scenarios are then confronted with the theory down to the details. Our study confirms the number of small galaxies that entered the cluster within the last few Gyr and the last significant merger. About 300 small galaxies ($M^* > 10^7$ M$_\odot$) entered the cluster recently, mostly within the last 500 Myr. In our previous dark matter-only studies, we showed that the simulated Virgo cluster accreted matter along a preferential direction, a filament, and that the last significant merger occurred during the last 3–4 Gyr. The group that finished merging within the last Gyr or so was about 10 per cent the mass of the cluster today. Recently, Lisker et al. (2018) proposed an observationally driven merging scenario according to which a group of about 10 per cent Virgo counterpart mass entered the cluster along the line of sight preventing us from seeing it directly today. They found it identifying in a phase-space diagram a clump of red galaxies with high velocities relative to the cluster centre but not in the inner core of the cluster. We identify the same group of galaxies in our simulation confirming both the result obtained in the dark matter-only regime and the observational findings. The group entered the cluster via the filament diametrically opposed to the centre of the box where the Milky Way counterpart is. The phase-space diagram produced with the simulated galaxies reveals an identical clump when positioning an observer in the line of sight of the infall direction of the group.

Overall, findings regarding the Virgo cluster, observational and numerical matches, and residual discrepancies between the observed cluster and its counterpart can be summarized as follows:

(i) Galaxies in the cluster core are in general redder and older.

(ii) The simulated Virgo cluster has an overall dynamical galaxy distributions matching the observed one with a virial radius of about 2.2 Mpc and a zero velocity radius of about 4.4 Mpc.

(iii) The galaxy luminosity and stellar mass distributions in the simulated Virgo cluster are in quite good agreement with the observed ones. The only exception being the inner core and the edges. However, edges might be affected by distance estimate uncertainties in the observational sample and the brightness of M87 might impact the observed inner core, observers deciding against observing them upon selection.

(iv) NUV–luminosity and stellar mass functions within, respectively, 0.15 and $\sim$3 Mpc obtained with the simulation match remarkably well the observations but at the faintest end in the first

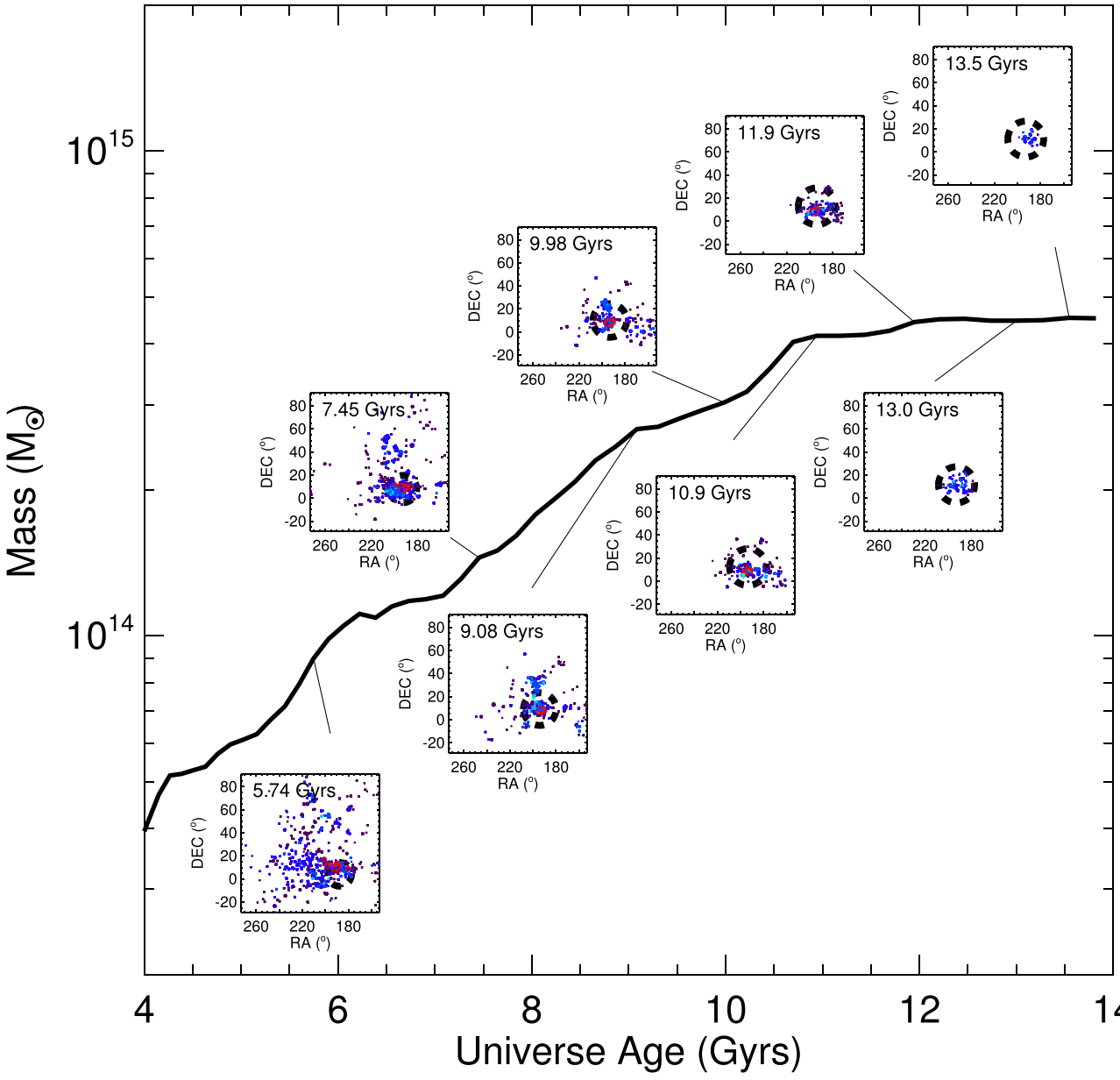

Figure 11. Merging history of the simulated Virgo cluster. Small insets show the position of the galaxies that will end up inside the virial radius of the cluster at redshift zero. The gradient of colour gives the status of the galaxy before entering the cluster: violet means that the galaxy was isolated, light blue stands for a satellite galaxy within a group. The red colour is used to highlight galaxies from the last significant merging group. The dashed black lines stand for the virial radius of the dark matter halo of the cluster at different epochs in angular coordinates. The factor derived at $z = 0$ to estimate the angular diameter given the distance of the cluster today is also used for earlier redshifts, in other words the simulated cluster is always seen by the fictive observer from the same distance that at $z = 0$. Galaxies within the cluster virial radius at a given time are not shown. The reconstruction of the Virgo cluster formation from observations is matched with good accuracy by the simulation: last significant merger quasi along the line of sight, quiet accretion lately and more active earlier on.

case. The mass resolution limit in the second case seems to be the only point of departure from the observational relation in the second case.

(v) The counterpart of M87 is quite a good match to the observed one. Still small discrepancies are visible and cannot be entirely accounted for by aperture radii: M87 clone appears slightly too massive (bright) and not enough red with respect to the real M87. Its stars are also too metal rich although of quite the proper age. Explorations will be made later regarding for instance the growth of the BH in M87 clone. Although more than big enough ($M > 10^{11} \mathrm{M}_{\odot}$), the BH indeed grew recently because of a merger. However, since a detailed comparison between the observed and the simulated BHs will have to be conducted carefully, in particular because of the physics used for the AGN feedback, for instance the cosmic ray physics is not included, it will be the subject of a future study.

(vi) There are two good candidates for being M49 and M60 clones though they also are slightly too blue.

(vii) The Virgo cluster counterpart has had a quiet merging history within the last few Gyr while it used to grow faster.

(viii) More precisely, Virgo counterpart underwent two major depressions in terms of galaxy accretions: first, about 7 Gyr ago, when it transitioned from an active agglomerator to a quieter one

in agreement with its cluster size and close by environment, and second, about 3 Gyr ago, when a small group congested the filament located directly on the opposite side from ours, thus preventing it from channelling matter on to the cluster.

(ix) Virgo counterpart accretes matter along that filament, a preferential direction.

(x) The last significant merging event was with the small congesting group. This group finished entering a bit more than a Gyr ago. It was about 10 per cent the mass of the cluster today.

This excellent numerical replica of the Virgo cluster of galaxies will permit studying more thoroughly the galaxy population of the cluster as well as the different galaxy types (jellyfish, backsplash, the fall-in small group, M87, etc.) in the cluster and comparing them directly with their observed counterparts to test different hydrodynamical modellings. Future studies will address the hot gas phase of the simulated cluster. Virgo is known to be a cool-core cluster and this property is most probably due to its history. It will be an excellent way of testing baryonic physics in the intracluster medium. Several properties like metallicity and temperature obtained in our simulated cluster are precious probes to investigate. The simulation of the Virgo cluster opens great prospectives and let us foresee multiple interesting projects. Moreover, a companion simulation to tackle residual differences highlighted in this paper is already currently running using the same kinetic stellar feedback but with metal yield curves and mass return times based on a Kroupa IMF.

ACKNOWLEDGEMENTS

This research has made use of the SIMBAD data base, operated at CDS, Strasbourg, France as well as of the Extragalactic Distance Database (http://edd.ifa.hawaii.edu). The authors gratefully acknowledge the Gauss Centre for Supercomputing e.V. (www.gauss-centre.eu) for providing computing time on the GCS Supercomputers SuperMUC at LRZ Munich. GY and AK acknowledge financial support from Ministerio de Ciencia, Innovación y Universidades/*Fondo Europeo de Desarrollo Regional*, under research grant PGC2018-094975-C21. AK further thanks Françoise Hardy for 'tant de belles choses'.

DATA AVAILABILITY

The authors will gladly share data regarding the galaxy population and dark matter haloes of the CLONE simulation of the Virgo cluster upon request.

REFERENCES

Adelman-McCarthy J. K. et al., 2009, ApJs, 175, 297
Aubert D., Pichon C., Colombi S., 2004, MNRAS, 352, 376
Avila-Reese V., Colín P., Gottlöber S., Firmani C., Maulbetsch C., 2005, ApJ, 634, 51
Baldry I. K., Glazebrook K., Driver S. P., 2008, MNRAS, 388, 945
Baldry I. K. et al., 2012, MNRAS, 421, 621
Bertschinger E., 1987, ApJ, 323, L103
Bertschinger E., 2001, ApJS, 137, 1
Binggeli B., Huchra J., 2000, in Murdin P., ed., Encyclopedia of Astronomy and Astrophysics, p. 1822
Binggeli B., Tammann G. A., Sandage A., 1987, AJ, 94, 251
Bistolas V., Hoffman Y., 1998, ApJ, 492, 439
Boselli A., Gavazzi G., 2014, A&AR, 22, 74
Boselli A., Boissier S., Cortese L., Gavazzi G., 2008, ApJ, 674, 742
Boselli A. et al., 2011, A&A, 528, A107
Boselli A. et al., 2014, A&A, 570, A69
Boselli A. et al., 2016a, A&A, 585, A2
Boselli A. et al., 2016b, A&A, 596, A11
Bruzual G., Charlot S., 2003, MNRAS, 344, 1000
Calvi R., Poggianti B. M., Vulcani B., Fasano G., 2013, MNRAS, 432, 3141
Corbett Moran C., Teyssier R., Lake G., 2014, MNRAS, 442, 2826
Côté P. et al., 2004, ApJS, 153, 223
de Vaucouleurs G., 1961, ApJS, 6, 213
Dekel A., Bertschinger E., Faber S. M., 1990, ApJ, 364, 349
Doumler T., Hoffman Y., Courtois H., Gottlöber S., 2013, MNRAS, 430, 888
Dubois Y., Teyssier R., 2008, A&A, 482, L13
Dubois Y., Devriendt J., Slyz A., Teyssier R., 2012, MNRAS, 420, 2662
Dubois Y., Volonteri M., Silk J., 2014a, MNRAS, 440, 1590
Dubois Y., Volonteri M., Silk J., Devriendt J., Slyz A., 2014b, MNRAS, 440, 2333
Dubois Y. et al., 2014c, MNRAS, 444, 1453
Dubois Y., Peirani S., Pichon C., Devriendt J., Gavazzi R., Welker C., Volonteri M., 2016, MNRAS, 463, 3948
Dubois Y. et al., 2020, preprint (arXiv:2009.10578)
Event Horizon Telescope Collaboration, 2019a, ApJ, 875, L1
Event Horizon Telescope Collaboration, 2019b, ApJ, 875, L2
Ferrarese L. et al., 2006, ApJS, 164, 334
Ferrarese L. et al., 2016, ApJ, 824, 10
Fisher K. B., Lahav O., Hoffman Y., Lynden-Bell D., Zaroubi S., 1995, MNRAS, 272, 885
Fixsen D. J., Cheng E. S., Gales J. M., Mather J. C., Shafer R. A., Wright E. L., 1996, ApJ, 473, 576
Forte J. C., Vega E. I., Faifer F., 2012, MNRAS, 421, 635
Fritz J., Hevics Collaboration, 2011, in Wang W., Lu J., Luo Z., Yang Z., Hua H., Chen Z., eds, ASP Conf. Ser. Vol. 446, Galaxy Evolution: Infrared to Millimeter Wavelength Perspective. Astron. Soc. Pac., San Francisco, p. 77
Ganon G., Hoffman Y., 1993, ApJ, 415, L5
Gebhardt K., Thomas J., 2009, ApJ, 700, 1690
Gil de Paz A. et al., 2007, ApJS, 173, 185
Haardt F., Madau P., 1996, ApJ, 461, 20
Hahn O., Abel T., 2011, MNRAS, 415, 2101
Hahn O., Martizzi D., Wu H.-Y., Evrard A. E., Teyssier R., Wechsler R. H., 2017, MNRAS, 470, 166
Hirschmann M., De Lucia G., Wilman D., Weinmann S., Iovino A., Cucciati O., Zibetti S., Villalobos Á., 2014, MNRAS, 444, 2938
Hoffman Y., Ribak E., 1991, ApJ, 380, L5
Hoffman Y., Ribak E., 1992, ApJ, 384, 448
Hoffman G. L., Olson D. W., Salpeter E. E., 1980, ApJ, 242, 861
Holmberg E., 1961, AJ, 66, 620
Huchra J. P., 1985, in Richter O.-G., Binggeli B., eds, European Southern Observatory Conference and Workshop Proceedings, Vol. 20. p. 181
Jasche J., Wandelt B. D., 2013, MNRAS, 432, 894
Karachentsev I. D., Kashibadze O. G., 2006, Astrophysics, 49, 3
Karachentsev I. D., Tully R. B., Wu P.-F., Shaya E. J., Dolphin A. E., 2014, ApJ, 782, 4
Kitaura F.-S., 2013, MNRAS, 429, L84
Kitaura F. S., Enßlin T. A., 2008, MNRAS, 389, 497
Kravtsov A. V., Vikhlinin A. A., Meshcheryakov A. V., 2018, Astron. Lett., 44, 8
Krumholz M. R., Tan J. C., 2007, ApJ, 654, 304
Lavaux G., 2016, MNRAS, 457, 172
Lavaux G., Mohayaee R., Colombi S., Tully R. B., Bernardeau F., Silk J., 2008, MNRAS, 383, 1292
Lee H.-R., Lee J. H., Jeong H., Park B.-G., 2016, ApJ, 823, 73
Li H., Gnedin O. Y., 2014, ApJ, 796, 10
Lisker T., Vijayaraghavan R., Janz J., Gallagher J. S., III, Engler C., Urich L., 2018, ApJ, 865, 40
Liu Y., Zhou X., Ma J., Wu H., Yang Y., Li J., Chen J., 2005, AJ, 129, 2628
Loubser S. I., Sánchez-Blázquez P., 2011, MNRAS, 410, 2679
McKinney J. C., Tchekhovskoy A., Blandford R. D., 2012, MNRAS, 423, 3083

McLeod D. J., McLure R. J., Dunlop J. S., Cullen F., Carnall A. C., Duncan K., 2021, MNRAS, 503, 4413
Maulbetsch C., Avila-Reese V., Colín P., Gottlöber S., Khalatyan A., Steinmetz M., 2007, ApJ, 654, 53
Olchanski M., Sorce J. G., 2018, A&A, 614, A102
Padmanabhan N. et al., 2008, ApJ, 674, 1217
Pappalardo C. et al., 2015, A&A, 573, A129
Peirani S., de Freitas Pacheco J. A., 2008, A&A, 488, 845
Peng E. W. et al., 2008, ApJ, 681, 197
Planck Collaboration XVI, 2014, A&A, 571, A16
Rasera Y., Teyssier R., 2006, A&A, 445, 1
Reaves G., 1956, AJ, 61, 69
Roediger J. C., Courteau S., McDonald M., MacArthur L. A., 2011a, MNRAS, 416, 1983
Roediger J. C., Courteau S., MacArthur L. A., McDonald M., 2011b, MNRAS, 416, 1996
Shakura N. I., Sunyaev R. A., 1973, A&A, 24, 337
Smith S., 1936, ApJ, 83, 23
Sorce J. G., 2015, MNRAS, 450, 2644
Sorce J. G., 2018, MNRAS, 478, 5199
Sorce J. G., Tempel E., 2017, MNRAS, 469, 2859
Sorce J. G., Courtois H. M., Gottlöber S., Hoffman Y., Tully R. B., 2014, MNRAS, 437, 3586
Sorce J. G. et al., 2016a, MNRAS, 455, 2078
Sorce J. G., Gottlöber S., Hoffman Y., Yepes G., 2016b, MNRAS, 460, 2015
Sorce J. G., Hoffman Y., Gottlöber S., 2017, MNRAS, 468, 1812
Sorce J. G., Blaizot J., Dubois Y., 2019, MNRAS, 486, 3951
Sorce J. G., Gottlöber S., Yepes G., 2020, MNRAS, 496, 5139
Struble M. F., Rood H. J., 1988, Sky Telesc., 75, 16
Sutherland R. S., Dopita M. A., 1993, ApJS, 88, 253
Taylor R., Davies J. I., Auld R., Minchin R. F., 2012, MNRAS, 423, 787
Teyssier R., 2002, A&A, 385, 337
Toro E. F., Spruce M., Speares W., 1994, Shock Waves, 4, 25
Tully R. B., Shaya E. J., Karachentsev I. D., Courtois H. M., Kocevski D. D., Rizzi L., Peel A., 2008, ApJ, 676, 184
Tully R. B. et al., 2013, AJ, 146, 86
Tully R. B., Courtois H. M., Sorce J. G., 2016, AJ, 152, 50
Tweed D., Devriendt J., Blaizot J., Colombi S., Slyz A., 2009, A&A, 506, 647
Umehata H. et al., 2019, Science, 366, 97
Vollmer B., Wong O. I., Braine J., Chung A., Kenney J. D. P., 2012, A&A, 543, A33
von der Linden A., Wild V., Kauffmann G., White S. D. M., Weinmann S., 2010, MNRAS, 404, 1231
Wang H., Mo H. J., Yang X., Jing Y. P., Lin W. P., 2014, ApJ, 794, 94
West M. J., Blakeslee J. P., 2000, ApJ, 543, L27
Wetzel A. R., Tinker J. L., Conroy C., 2012, MNRAS, 424, 232
Wong O. I., Kenney J. D. P., 2009, in Sheth K., Noriega-Crespo A., Ingalls J. G., Paladini R., eds, The Evolving ISM in the Milky Way and Nearby Galaxies. p. 66
Zaroubi S., Hoffman Y., Dekel A., 1999, ApJ, 520, 413
Zhu L. et al., 2014, ApJ, 792, 59

APPENDIX A: DM VERSUS HYDRO RUN

This appendix intends to demonstrate that the hydrodynamic component of the simulation did not perturb beyond its normal effect the dark matter result. Fig. A1 (top) confirms that the final virial mass of the cluster is similar with and without gas after rescaling to account for the baryonic content and that there are only moderate changes in the assembly history especially recently. The bottom of the same figure shows that indeed hydrodynamics suppresses the small mass haloes but does not affect the high-mass end of the dark matter halo mass function.

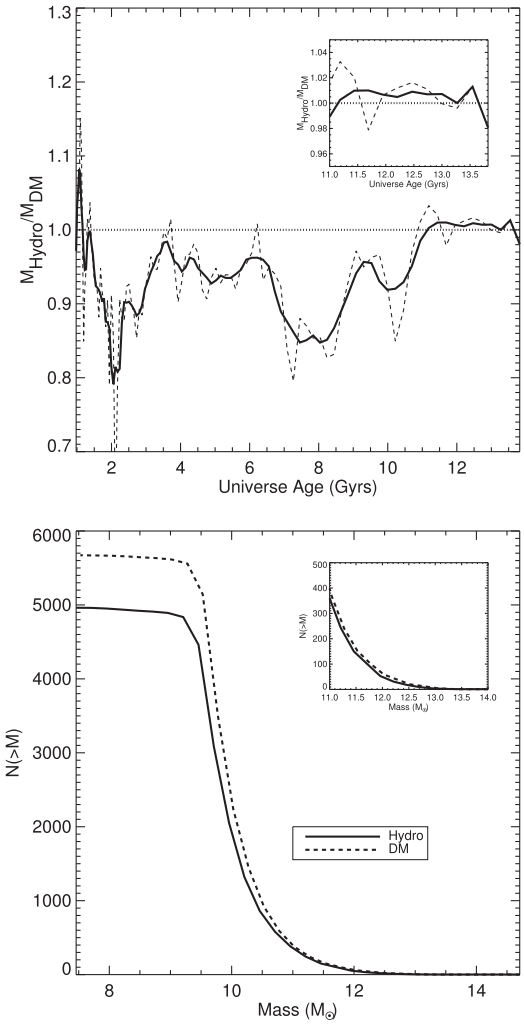

Figure A1. Comparisons between two runs with the same parameters and same initial conditions but one with gas (Hydro), the other without (DM). Top: Ratio of the total virial mass of the haloes in both runs as a function of time (after accounting for the baryonic content in the hydrodynamical run). The dashed line is obtained considering each snapshot while the solid line is a mean across five snapshots. Bottom: Halo mass functions in both runs. Adding gas suppresses small mass haloes but does not impact the high-mass end of the function as expected.

APPENDIX B: CLUSTER-CENTRIC VELOCITIES

To compute cluster-centric velocity with the help of Fig. B1 and Karachentsev & Kashibadze (2006), let C be the centre of a system of galaxies located at the distance D and receding with a velocity V from us. Consider a galaxy N at the distance D_N and receding at V_N from us. We call the angular separation, between the centre of the system and the galaxy N, θ. Then, the distance between the galaxy N and the centre of the system R_c can be expressed as follows:

$$R_c = R = \sqrt{D^2 + D_N^2 - 2DD_N\cos\theta}\,. \tag{B1}$$

The galaxy N is going away from C at the velocity:

$$V_c = V_N\cos\lambda - V\cos\mu\,, \tag{B2}$$

where $\mu = \lambda + \theta$ and $\tan\lambda = \frac{D\sin\theta}{D_N - D\cos\theta}$ assuming that random peculiar velocities are low compared to expansion velocities.

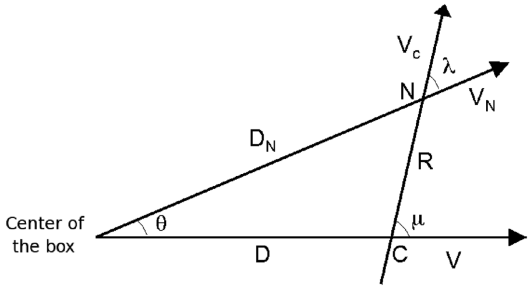

Figure B1. Diagram representing the different parameters required to compute the distance and the velocity of a galaxy with respect to the centre of a system.

APPENDIX C: ZERO VELOCITY RADIUS

The zero velocity radius is a priori the intersection of the running median with the *X*-axis. However, because of a high velocity dispersion in cluster cores, running medians are noisier close to the cores than in the far outskirts where the Hubble flow is reached. Consequently, we fit the running median with a theoretical velocity profile derived from the spherical model by Peirani & de Freitas Pacheco (2008). This profile assumes a spherical collapse model, Λ included, in the outskirts of the clusters. In the core, assumed to contain most of the mass where shell crossing has already happened, the orbits are mainly radial. Then:

$$V(R_c) = 1.377 H_0 \times R_c - 0.976 \times \frac{H_0}{R_c^n} \times \left(\frac{GM}{H_0^2}\right)^{\frac{n+1}{3}} \quad \text{(C1)}$$

with M the core cluster mass, R_c the distance of the galaxy to the cluster centre, $V(R_c) = V_c$ the radial velocity of the galaxy with respect to the cluster centre, and $n = 0.627$ at $z = 0$. By definition, the velocity at the zero velocity radius is null. Because the model is valid only up to the point where the Hubble flow is reached, fits are based on the left end of the running median where cores and outskirts are in close contact with each other. We proceed iteratively until the portion of the running median to fit is delimited such that the model converges to the data.

APPENDIX D: COMPLETENESS OF THE SIMULATION

Fig. D1 top shows the completeness of the simulation at $M^* = 10^{8.5}$ $M_\odot$. This sets the limit of validity of the close comparisons between observations and simulations in this paper without correction for completeness. To evaluate the correction, we fit a double Schechter function to the galaxy stellar mass function within the 12 Mpc radius spherical volume of the simulation using only points above the completeness limit (e.g. McLeod et al. 2021):

$$\Phi(M) = \ln(10)\exp[-10^{(M-M^*)}]10^{(M-M^*)}[\Phi_1^* 10^{(M-M^*)\alpha_1} + \Phi_2^* 10^{(M-M^*)\alpha_2}] \quad \text{(D1)}$$

We use as a first proxy the parameters from Baldry et al. (2012) who derived galaxy stellar mass functions in the local Universe. We increase M^* following Calvi et al. (2013) who found that M^* evolves with the environment density and Φ_2^* following Baldry, Glazebrook & Driver (2008) who observed steeper slopes at the low-mass end in clusters than in the field. These parameters are adjusted to fit only the points above the completeness limit as shown in Fig. D1 (bottom). Finally, $M^* = 11$, $\log(\Phi_1^*) = -2.4$, $\log(\Phi_2^*) = -2.1$, $\alpha_1 = -0.35$, $\alpha_2 = -1.5$.

Typically about 10 000–12 000 (50–60) small galaxies of $M^* > 10^7$ $M_\odot$ are missed in the 12 Mpc radius spherical volume (simulated Virgo cluster) given the parameters used for the halo finder run and the resolution of the simulation.

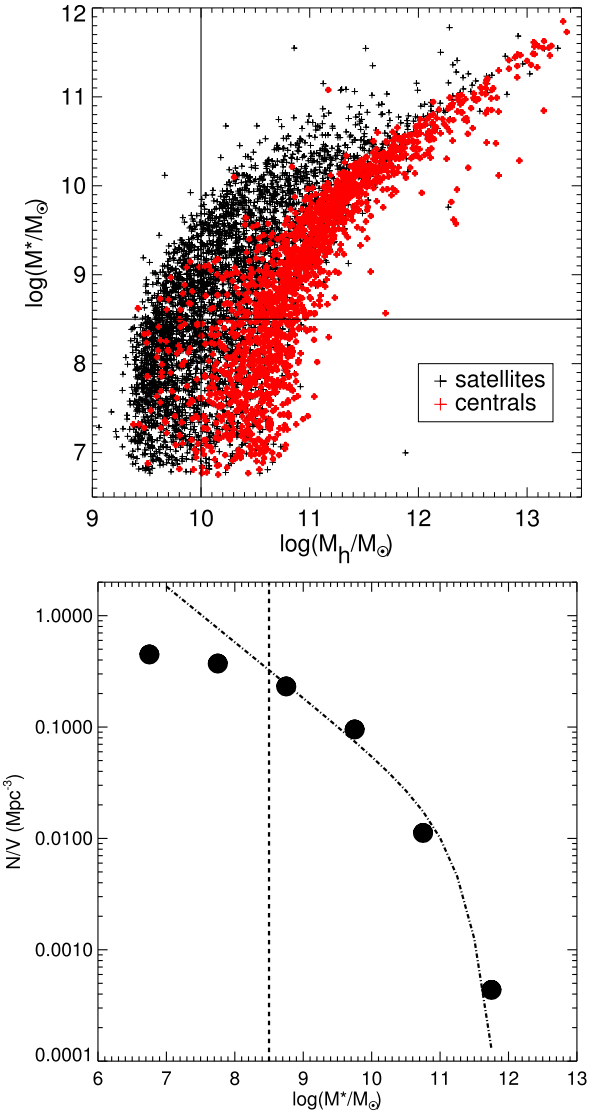

Figure D1. Top: Stellar mass as a function of dark matter halo mass for central (red crosses) and satellite (black crosses) galaxies in the 12 Mpc radius spherical volume. Bottom: Galaxy stellar mass function of the 12 Mpc radius spherical volume (filled circles) fitted with a double Schechter function (dot–dashed line). The completeness is visible at $M^* = 10^{8.5}$ $M_\odot$.

This paper has been typeset from a TEX/LATEX file prepared by the author.